

Effects of waveform systematics on inferences of neutron star population properties and the nuclear equation of state

Anjali B. Yelikar*

*Rochester Institute of Technology, Rochester, New York 14623, USA and
Vanderbilt University, Nashville, TN 37235, USA*

Richard O’Shaughnessy

Rochester Institute of Technology, Rochester, New York 14623, USA

Daniel Wysocki

University of Wisconsin-Milwaukee, Milwaukee, WI 53201, USA

Leslie Wade

Kenyon College, Gambier, Ohio 43022, USA

(Dated: October 21, 2024)

Gravitational waves from inspiralling neutron stars carry information about matter at extreme gravity and density. The binary neutron star (BNS) event GW170817 provided, for the first time, insight into dense matter through this window. Since then, another BNS (GW190425) and several neutron star-black hole events have been detected, although the tidal measurements were not expected to be well-constrained from them. Collective information regarding the behavior of nuclear matter at extreme densities can be done by performing a joint population inference for the masses, spins, and equation-of-state [1] to enable better understanding. This population inference, in turn, relies on accurate estimates of intrinsic parameters of individual events. In this study, we investigate how the differences in parameter inference of BNS events using different waveform models can affect the eventual inference of the nuclear equation-of-state. We use the state-of-the-art model TEOBRESUMS with IMRPHENOMD_NRTIDALV2 as a comparison model.

I. INTRODUCTION

Neutron stars have proved to be excellent laboratories for understanding the behavior of cold nuclear matter, be it observations in the electromagnetic spectrum or gravitational waves. The ground-based gravitational wave detectors, LIGO-Virgo-KAGRA (LVK) [2–4], have observed about 90 signals from binary mergers till March 2020 since the first detection in September 2015 [5–8]. The most recent population paper from the LVK collaboration paper [9] estimated the merger rate of binary neutron stars to be between 10 and 1700 $\text{Gpc}^{-3}\text{yr}^{-1}$. To date, only two confirmed BNS have been found in the gravitational wave domain- GW170817 [10] and GW190425 [11]. Gravitational wave measurements from GW170817 alone were able to place constraints on existing EOS models [12–17]. The observations from its electromagnetic counterpart, AT2017gfo, crucial in identifying the sky localization and distance with certainty, also provided additional information from which to understand the interior of neutron stars better [18–22]. Direct observations of pulsars alone in various regions of the EM spectrum and results from the NICER experiment have provided insight regarding the interior of neutron stars, helping constrain their mass-radius relationship and in turn helping understand which of the

equation of state models accurately predict the results from observed data [23–27]. Joint constraints from GW and EM observations have also been insightful in providing better constraints on existing EoS models [28].

Gravitational waves from neutron stars also provide support for the existence of higher mass NS in contrast to the neutron stars observed in Galactic BNS. We expect to see many more BNSs with improving sensitivity of current and next generation GW detectors [29], and combining information from future detections will enable better constraints on the pressure-density behavior of high-density matter, hence providing an understanding and validity of existing equation-of-state models from gravitational wave information alone. In a follow-up paper on the discovery of GW170817 [30], information from gravitational waves was used to constrain the neutron star radius and the nuclear equation of state.

In Wysocki et al. [1], simultaneous measurement of mass and spin distributions along with the equation of state (EoS) was demonstrated with a set of fiducial binary neutron star merger signals. The study used the Bayesian population inference code, POPMODELS [31], and a spectral representation for the equation of state introduced by Lindblom [32]. Based on this work, we propose to investigate the effect of waveform systematics on the joint inference of NS population properties and the EoS. Similar hierarchical inference techniques involving stacking gravitational wave information from binary neutron stars have been described in [33, 34].

* ay2016@rit.edu

This paper is organized as follows. In Section II, we review the gravitational wave parameter inference tool RIFT and population inference tool POPMODELS; the source population model and waveform models assumed. We describe one fiducial set of synthetic sources populated using astrophysically motivated models. In Section III, we present comparisons of the performance of PE using different waveform models and quantify these differences with techniques also used in [35]. We further investigate the equation of state results inferred from a joint population and EoS analyses. We show that waveform modeling uncertainties will be significant when combining information from multiple detections to infer the properties of a neutron star. In Section IV, we evaluate our results within the context of existing literature. In Section V, we summarize our results and discuss their potential applications to future detections of BNS sources and improvements in our current setup, such as combining information from neutron star-black hole (NSBH) sources.

II. METHODS

A. RIFT review

A coalescing compact binary in a quasi-circular orbit can be entirely characterized by its intrinsic and extrinsic parameters. By intrinsic parameters, we refer to the binary’s detector-frame masses m_i , spins χ_i , and any quantities characterizing matter in the system, Λ_i . By extrinsic parameters, we refer to the seven numbers needed to characterize its spacetime location and orientation; luminosity distance (d_L), right ascension (α), declination (δ), inclination (ι), polarization (ψ), coalescence phase (ϕ_c), and time (t_c). We will express masses in solar mass units and dimensionless nonprecessing spins in terms of cartesian components aligned with the orbital angular momentum $\chi_{i,z}$, as we use waveform models that do not account for precession. We will use $\boldsymbol{\lambda}$ and θ to refer to intrinsic and extrinsic parameters.

$$\boldsymbol{\lambda} : (\mathcal{M}, q, \chi_{1,z}, \chi_{2,z}, \Lambda_1, \Lambda_2)$$

$$\theta : (d_L, \alpha, \delta, \iota, \psi, \phi_c, t_c)$$

RIFT [36, 37] consists of a two-stage iterative process to interpret gravitational wave data d via comparison to predicted gravitational wave signals $h(\boldsymbol{\lambda}, \theta)$. In one stage, for each λ_β from some proposed “grid” $\beta = 1, 2, \dots, N$ of candidate parameters, RIFT computes a marginal likelihood

$$\mathcal{L}_{\text{marg}} \equiv \int \mathcal{L}(\boldsymbol{\lambda}, \theta) p(\theta) d\theta \quad (1)$$

from the likelihood $\mathcal{L}(\boldsymbol{\lambda}, \theta)$ of the gravitational wave signal in the multi-detector network, accounting for detector

response; see the RIFT paper for a more detailed specification [36, 37]. In the second stage, RIFT performs two tasks. First, it generates an approximation to $\mathcal{L}(\boldsymbol{\lambda})$ based on its accumulated archived knowledge of marginal likelihood evaluations ($\lambda_\beta, \mathcal{L}_\beta$). Gaussian processes, random forests, or other suitable approximation techniques can generate this approximation. Second, using this approximation, it generates the (detector-frame) posterior distribution

$$p_{\text{post}} = \frac{\mathcal{L}_{\text{marg}}(\boldsymbol{\lambda}) p(\boldsymbol{\lambda})}{\int d\boldsymbol{\lambda} \mathcal{L}_{\text{marg}}(\boldsymbol{\lambda}) p(\boldsymbol{\lambda})}. \quad (2)$$

where prior $p(\boldsymbol{\lambda})$ is prior on intrinsic parameters like mass and spin. The posterior is produced by performing a Monte Carlo integral: the evaluation points and weights in that integral are weighted posterior samples, which are fairly resampled to generate conventional independent, identically distributed “posterior samples.” For further details on RIFT’s technical underpinnings and performance, see [36–39].

To facilitate robust sampling of the most a priori important regions, particularly in NS tidal deformability Λ_i , RIFT further adopts a hierarchical strategy, employing targeted sampling priors for early iterations to guarantee thorough coverage. As described in prior work [37], the initial range of Λ_i used to construct the first set of likelihood training data uses an interval in $\Lambda(m)$ between $\min[50, 0.2\Lambda_{\text{fid}}(m)]$ and $\max(150, 2\Lambda_{\text{fid}}(m))$, where $\Lambda_{\text{fid}} = 3000((2.2 - m/M_\odot)/1.2)^2$. This choice guarantees comprehensive sampling over the range of Λ , most likely to be consistent with physically plausible EoS. To cover the low- Λ region further, the next few iterations adopt a nonuniform triangular prior in Λ_i , which goes to zero at the maximum allowed value. After these first few iterations establish seed training data, subsequent iterations are repeated using the target inference priors, until the posterior converges.

B. Waveform models and analysis settings

The tidal waveform models used in this study are IMRPHENOMD_NRTIDALV2 and TEOBRESUMS. NR-Tidalv2 models [40] are improved versions of NR-Tidal [41] models, which are closed-form tidal approximants for binary neutron star coalescence and have been analytically added to selected binary black hole GW model to obtain a binary neutron star waveform, either in the time or frequency domain. TEOBRESUMS [42] is another but unique time-domain EOB formalism that includes tidal effects for all modes $\ell \leq 4$, but no $m = 0$ and models tidal effect up to $\Lambda_{1,2} < 5000$ and for spins up to 0.5.

For parameter inference, we use TEOBRESUMS for injections and recovery and IMRPHENOMD_NRTIDALV2 for the recovery, starting the signal evolution and likelihood integration at 20Hz, performing all analysis with

4096Hz time series in Gaussian noise with known advanced LIGO design PSDs [43]. The BNS signal is generated for 4096 seconds but analysis was performed only on 256 seconds of data. For each synthetic event and interferometer, we use the same noise realization for all waveform approximations. Therefore, the differences between them arise solely due to waveform systematics. TEOBRESUMS and IMRPHENOMD_NRTIDALV2 approximants are used with $\ell = 4$ and $\ell = 2$ settings respectively.

C. PopModels review

To jointly infer both the nuclear EoS and NS-NS population, we use the framework introduced in two previous works led by Wysocki [1, 44], which we denote as “bayesian parametric models” (henceforth denoted as BPM). Within this framework, binaries with intrinsic parameters λ merge at a rate $\mathcal{R}p(\lambda)$. Generally the merger rate \mathcal{R} and population distribution p depend on population and EoS hyperparameters X . BPM’s inputs are (a) the underlying parameterized population model $p(\lambda|X)$, $\mathcal{R}(X)$ and (b) an estimate $\mu(X)$ of how many events a given experiment should find on average. Following BPM, we estimate this rate using a characteristic sensitive 4-volume denoted $VT(\lambda)$. In terms of these ingredients, BPM expresses the likelihood of an astrophysical BBH population with parameters X as a conventional inhomogeneous Poisson process:

$$\mathcal{L}(\mathcal{R}, X) \propto e^{-\mu(\mathcal{R}, X)} \prod_{n=1}^N \int d\lambda \ell_n(\lambda) \mathcal{R}p(\lambda | X), \quad (3)$$

where $\mu(\mathcal{R}, X)$ is the expected number of detections under a given population parameterization X with overall rate \mathcal{R} and where $\ell_n(x) = p(d_n|x)$ is the likelihood of data d_n —corresponding to the n th detection—given binary parameters x . Like previous EoS inferences within this framework [1], all single-event marginal likelihoods ℓ_n are provided by interpolating the training likelihood data provided by conventional RIFT single-event inference.

We employ precisely the same NS population model proposed in previous work with BPM on EoS [1]. Specifically, motivated by observations of galactic binary neutron stars [45, 46], we employ a two-component population of neutron stars, with overall minimum and maximum masses set by the nuclear equation of state:

$$p(x) \propto \sum_{k=1}^K w_k \mathcal{M}_k(m_1) \mathcal{M}_k(m_2) \mathcal{S}_k(\chi_{1,z}) \mathcal{S}_k(\chi_{2,z}) \quad (4)$$

everywhere that $m_{\min}(\gamma) \leq m_1 \leq m_2 \leq m_{\max}(\gamma)$ and $\Lambda_i = \Lambda(m_i, \gamma)$, and zero elsewhere. \mathcal{M}_k and \mathcal{S}_k represent the mass and spin distributions for the k th sub-population, respectively. We model the \mathcal{M}_k ’s as Gaussians with unknown mean and variance. The \mathcal{S}_k ’s are

assumed to follow beta distributions bounded by $|\chi_z| < 0.05$, again with unknown mean and variance. For simplicity’s sake, we assert that the means and variances don’t change between the primary and secondary NS. The $\Lambda_i = \Lambda(m_i, \gamma)$ constraint introduces delta functions into the expression for $p(x)$

D. Equation of state representation

In this work we adopt the spectral EoS parameterization introduced by Lindblom [47], implemented in Carney et al [48] in LALSUITE [49], and previously used to interpret GW170817 [30]. In this specific representation, the nuclear equation of state relating energy density ϵ and pressure p is characterized by a low-density SLy EoS joined to a spectral representation at $p_0 = 5.4 \times 10^{32} \text{dyne cm}^{-2}$, using a high-density four-parameter spectral model characterized by its adiabatic index $\Gamma(p)$:

$$\ln \Gamma(p) = \sum_{k=0}^3 \gamma_k [\ln(p/p_0)]^k, \quad (5)$$

where γ_k are expansion coefficients.

We employ the already-deployed POPMODELS interface to the underlying lalsuite implementation of this equation of state. As a fiducial EoS, we will adopt the spectral approximation to APR4 from Lindblom [47], given by $\gamma_0 = 0.8651$, $\gamma_1 = 0.1548$, $\gamma_2 = -0.0151$, $\gamma_3 = -0.0002$. All of our analyses use uninformative uniform priors on the spectral EoS parameters, following previous work [1, 30, 48]; γ_0 : U[0.2, 2], γ_1 : U[-1.6, +1.7], γ_2 : U[-0.6, +0.6], γ_3 : U[-0.02, +0.02].

The pressure and nuclear density of the neutron star’s interior are modeled by spectral parameterization.

E. Fiducial injections and Source population model

We consider one universe of 100 synthetic signals for a 2-detector network (HL), with signals populated from the following model. For our fiducial model, we took a two-component ($K = 2$ in Eq.) mass distribution based on the galactic neutron star constraints from Alsing *et al.* [46], in the first row of Table 3. Rather than take their maximum a posteriori values, we approximated their reported estimates as Gaussians, and took a single draw, resulting in $\mathbb{E}[m]_1 = 1.34 M_\odot$, $\text{Std}[m]_1 = 0.05 M_\odot$, $\mathbb{E}[m]_2 = 1.88 M_\odot$, $\text{Std}[m]_2 = 0.32 M_\odot$, and relative weights of 6 : 4. For the low mass component’s spin distribution, we utilize a zero-spin model, attainable using a β distribution with $\mathbb{E}[\chi_z]_1 = 0$ and $\text{Std}[\chi_z]_1 \rightarrow 0$. For the high mass component, however, we expect higher spins, as these would likely be recycled pulsars [50], and so we adopt fiducial choices $\mathbb{E}[\chi_z]_2 = 0.02$ and $\text{Std}[\chi_z]_2 = 0.01$.

Our population analyses use uninformative priors, uniform (U) in $\mathbb{E}[m]$, $\mathbb{E}[\chi_z]$, $\text{Std}[m]$, and log-uniform (LU) in

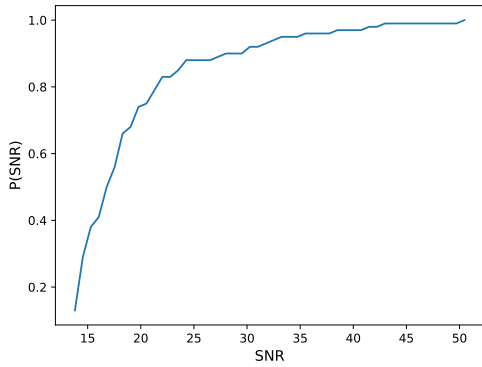


FIG. 1. Cumulative SNR distribution for a synthetic population of 100 events each drawn from the fiducial BNS populations described in Sec. II C. To avoid ambiguity, this figure shows the expected SNR (i.e., the SNR evaluated using a zero-noise realization).

each sub-population’s rate and $\text{Std}[\chi_z]$; \mathcal{R} [$\text{Gpc}^{-3} \text{yr}^{-1}$]: LU $[1, 10^5]$, $\mathbb{E}[m]$ [M_\odot]: U $[0.9, 2.9]$, $\text{Std}[m]$ [M_\odot]: LU $[0.05, 5]$, $\mathbb{E}[\chi]$: U $[-0.05, +0.05]$ and $\text{Std}[\chi]$: U $[0, 0.05]$. To account for observations of galactic neutron stars, rather than reanalyze all galactic observations ourselves, we employ pre-digested prior constraints on this same two-component mass model provided by Table 3 of [46]. In particular, we use an (improper) prior in the maximum neutron star mass $m_{\text{max}}(\gamma)$, extending from $1.97M_\odot$ to infinity, to account for the impact of the most recent well-determined NS masses on the inferred NS maximum mass [51–53].

Figure 1 shows the cumulative SNR distribution (under a “zero-noise” assumption) of the specific synthetic population generated from this distribution. Compared to GW170817’s confident detection, which was a BNS merger that occurred at 40Mpc detected by LIGO-Virgo with a SNR of 32.4, the majority of the signals in this fiducial population have SNRs below or near the typical detection criteria for a BNS merger, with some having high enough amplitudes.

III. RESULTS

In our calculations, we first construct a single large synthetic sample of merging binary NS drawn from our population model, weighted by their probability of detection. In this work, we have constructed our synthetic population using the TEOBResumS waveform model. Rather than regenerate many small independent synthetic universes, we then conceive of experiments in which different subsets of our full sample are identified via a GW survey. Thus, for each member of our large synthetic sample, we have performed full source parameter inference with RIFT in an EoS-agnostic phenomenological form, providing the underlying training data $\{\lambda_\alpha, \ln \mathcal{L}_{\text{marg}}(\lambda_\alpha)\}$

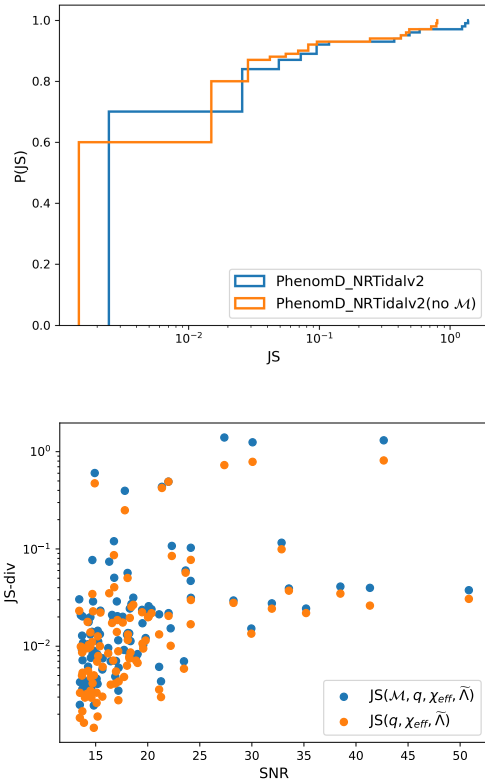


FIG. 2. *Top panel:* JS-divergence values of parameters \mathcal{M}_c , q , χ_{eff} and $\tilde{\Lambda}$ distribution for analysis on IMRPHENOMD_NRTIDALV2 with TEOBRESUMS-lmax4 injections. *Bottom panel:* Scatter plot showing how the zero-noise SNR of the injections from the population relates to the JS divergence value between TEOBRESUMS and IMRPHENOMD_NRTIDALV2 samples for the parameters noted in the legend.

used to interpolate the RIFT log-likelihood over λ .

A. Single event parameter inference

Any systematic effect of source model waveforms on EoS and population inference must be inherited from source parameter inference. In this section, we briefly review the similarities and differences between different interpretations of synthetic events, depending on the waveform model used.

We quantify the differences between the various parameter estimation analyses using Jensen-Shannon (JS) divergences. The divergence values shown are the summation of individual JS divergence values for the parameters \mathcal{M}_c , q , χ_{eff} and $\tilde{\Lambda}$. The top panel of Figure 2 shows the CDF of the JS-divergences for IMRPHENOMD_NRTIDALV2 with TEOBRESUMS-lmax4 injections, and about 20% of the population has values greater than 0.1. These substantial differences persist

even if our JS divergence omits the chirp mass. In other words, for many events, these two waveform models draw notably different conclusions about astrophysically pertinent parameters.

The bottom panel of Figure 2 provides a scatterplot of the JS divergence versus the expected SNR for each injection (assessed using a zero-noise realization). Notably, large JS can occur at any signal amplitude, including near the detection threshold; however, at large signal amplitude, the JS divergence is never small. This trend suggests that systematics can be important for any signal amplitude (i.e., $JS > 10^{-2}$), though they will be ubiquitously important for sources with $SNR \gtrsim 25$.

As a concrete example, Figure 3 shows two inferences of the same binary. This binary has a relatively large total mass but a modest signal amplitude of 22.31, with a peak marginal log-likelihood of only 200, about half of GW170817's peak. In both cases, the tidal deformability is poorly constrained to an interval in excess of what any plausible EoS would support. However, within the context of the even broader range of possibilities allowed by our purely phenomenological tidal parameterization, in which Λ_i are uniformly and independently distributed between $[0, 5000]$, these two inferences do differ notably in their conclusions about $\tilde{\Lambda}$.

The example shown in Figure 3 also highlights a critical feature of real PE and the propagation of systematics into population inference. Because of the choice of priors adopted for real PE, that inference may (or may not) exhibit substantial differences between different models. By contrast, all the EoS models that we consider would predict only very small $\tilde{\Lambda}$ in this mass range. As a result, the JS divergence (though a useful guide to identifying coarse model differences) doesn't reflect our prior knowledge about what physics can support at these high masses. Figure 4 shows the same analysis as Figure 3, now focused on a smaller range of $\tilde{\Lambda}$. In this focused range, the two analyses exhibit even larger differences in their marginal posterior for $\tilde{\Lambda}$ and in the likelihood evaluations used to draw that conclusion (see, e.g., the differences in red points between the left and right figure). This focused representation highlights the fact that the impact of systematics is highly uneven across the posterior, and small differences globally may disguise larger differences on smaller but physically critical scales.

B. Population inference: An extreme scenario

For the joint population and equation-of-state inference, we selected ten events whose JS-divergences values from PE were highest between TEOBRESUMS and IMRPHENOMD_NRTIDALV2. Two sets of such analyses were performed— one for each of the waveform models assumed in PE. Ensuring convergence of the analyses, we then looked at the radius and tidal deformability distribution of a $1.4M_{\odot}$ neutron star for the various EoSs inferred from the population analy-

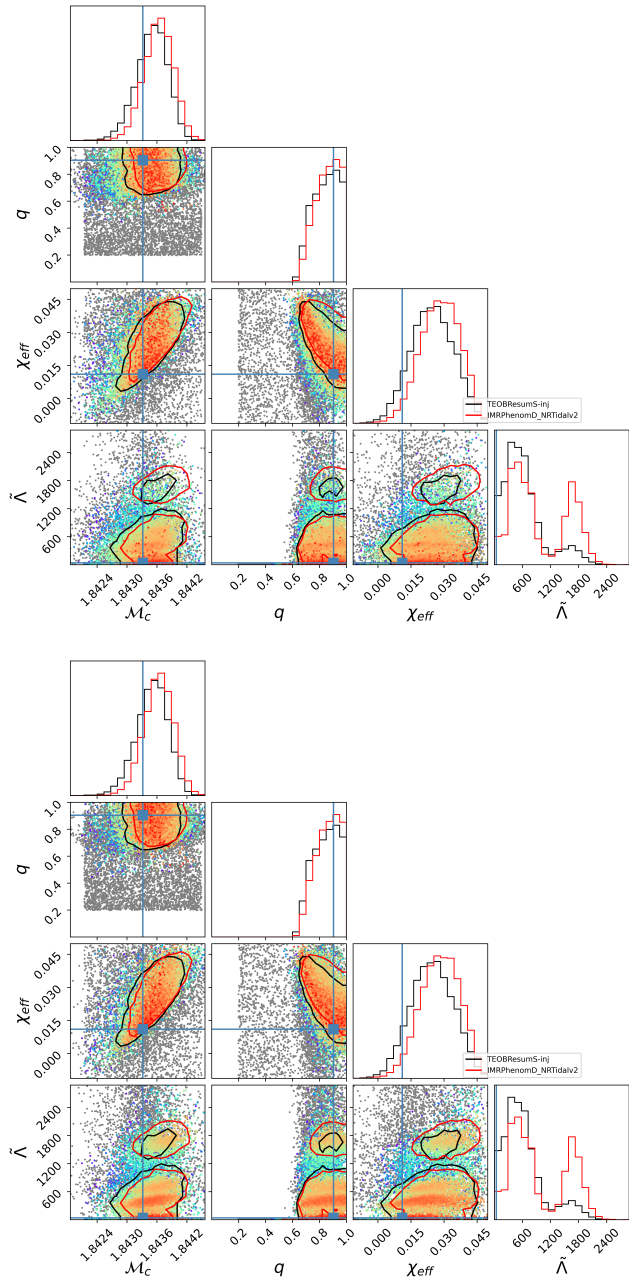


FIG. 3. Corner plots showing recovered 1D distributions of \mathcal{M}_c , q , χ_{eff} and $\tilde{\Lambda}$ for a TEOBRESUMS injection (cross-hairs indicate true value) analyzed with various waveform models listed in the legend. *Top panel*: Colored grid points from the TEOBRESUMS run. *Bottom panel*: Colored grid points from the IMRPHENOMD_NRTIDALV2 run. The four-parameter JS-divergence value between TEOBRESUMS and IMRPHENOMD_NRTIDALV2 for this event is 0.107.

ses. Although Fig. 6 shows that the information from both analyses differs very little, they are important enough to exhibit systematics for other parameters. Figure 5 shows a significant difference between the inferred radius and tidal deformability from the two

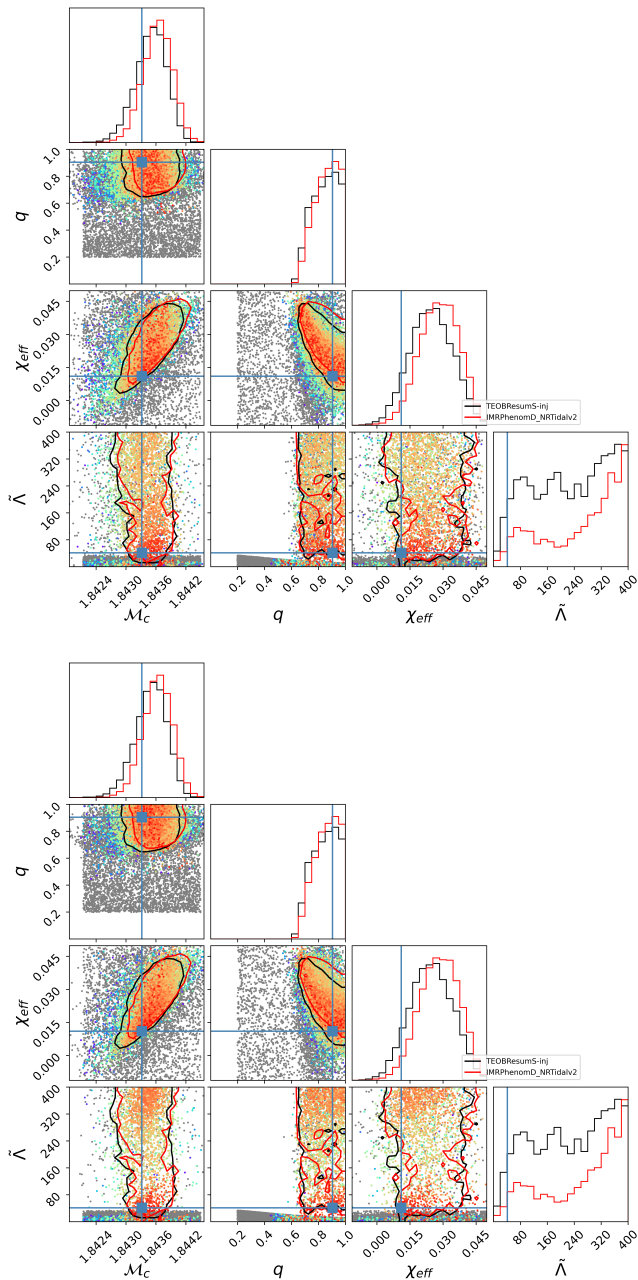


FIG. 4. Corner plot showing recovered 1D distributions of \mathcal{M}_c , q , χ_{eff} and $\tilde{\Lambda}$ for a TEOBRESUMS injection (cross-hairs indicate true value) analyzed with various waveform models listed in the legend, the same event as in Fig. 3 but with a narrower plotting range on the tidal deformability parameter. *Top panel*: Colored grid points from the TEOBRESUMS run. *Bottom panel*: Colored grid points from the IMRPHENOMD_NRTIDALV2 run

analyses. TEOBRESUMS consistently infers a smaller radius and tidal deformability compared to IMRPHENOMD_NRTIDALV2 in this scenario. The TEOBRESUMS model predicts a median NS radius of $R_{0.5} = 12.16$ km with a standard deviation of 0.17 km while for IMR-

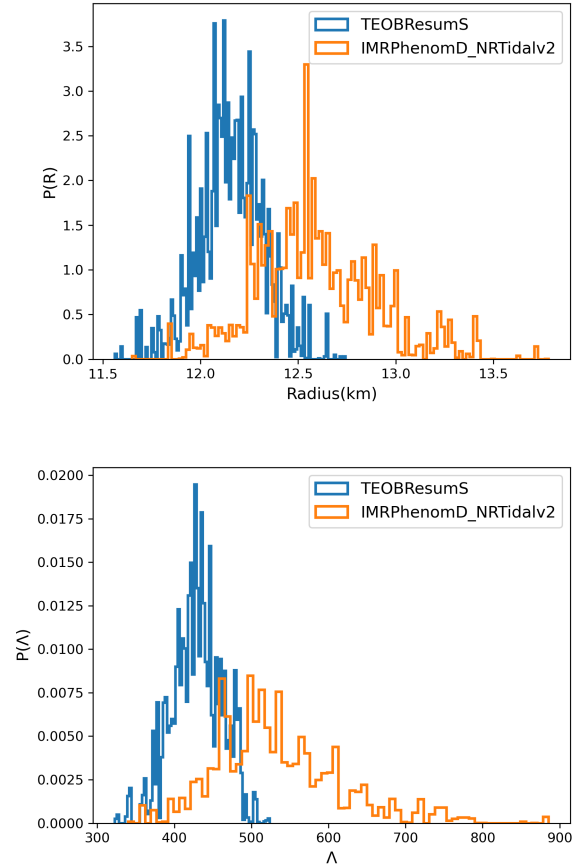


FIG. 5. *Top panel*: Posterior distribution for the radius of a typical $1.4M_{\odot}$ neutron star for the equations-of-state realizations from the joint population and EoS inference. *Bottom panel*: Posterior distribution of the dimensionless tidal deformability of a $1.4M_{\odot}$ neutron star for the equations-of-state realizations from the joint population and EoS inference. Legend indicates the waveform model that was used in the PE for the respective population analyses.

PHENOMD_NRTIDALV2 they are 12.55 km and 0.31 km, respectively, meaning the inferred radius differs by 2σ in one case. The tidal deformability distributions also show a similar trend with $\tilde{\Lambda}_{0.5}=429.28$, $\sigma=32.35$ for TEOBRESUMS and $\tilde{\Lambda}_{0.5} = 519.428$, $\sigma=81.69$ for IMRPHENOMD_NRTIDALV2. The $R_{1.4}$ and $\Lambda_{1.4}$ distribution for IMRPHENOMD_NRTIDALV2 also have a wider spread compared to TEOBRESUMS.

For both of our analyses of the same fiducial ten-event sample, we also calculate the rest mass density versus pressure trends from the inferred adiabatic index coefficients. Figure 6 plots the ratio of pressure estimates from the recovered EoSs to that of pressure estimates from a fiducial reference EoS (APR). We limit ourselves to densities less than $3 \times 10^{15} \text{ g cm}^{-3}$. For comparison, we also show the results inferred from the original LVK interpretation of GW170817 [54], derived from hyperparameter samples using the same spectral EoS parameterization

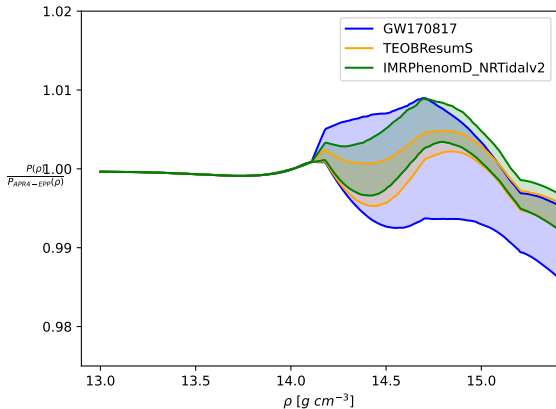


FIG. 6. Pressure-density plot comparing population analyses results from the different parameter estimation results performed for the same TEOBRESUMS-lmax4 injection waveform model indicated in the legend. Specifically, it plots the ratio of pressure estimates from the recovered EoSs to that of pressure estimates from the injected equation-of-state, APR4. The shaded region indicates the 90% CI of the respective analyses.

and implementation. [For efficiency, these samples were also used to initialize our population inference calculations.] As expected, the GW170817 EoS posterior encompasses the inferences derived using both waveform models. Too, inferences derived using the two waveform models differ modestly at moderate density, consistent with the modest differences seen for fiducial NS radius in Figure 5.

As demonstrated qualitatively in Figure 2 and Figure 10 in the Appendix, the ten events identified here are not exceptional in signal amplitude nor source parameters. Many sources have only modestly lower JS divergence than the events identified here. Therefore, we expect that while this analysis highlights a relatively unlikely scenario, it remains suggestive of a broader issue: a long tail of events with large systematics, where those systematics cannot be identified save by analysis with multiple waveform families. When incorporated into a population study, these events will impact our global conclusions about source parameters in proportion to the fraction of such events included.

C. Population analysis: Representative samples

To compare against our choice of picking events with large differences in PE between waveform models, we also perform similar population analyses but with two random choices of 10 events from the population, i.e., without taking the JS divergences value into consideration. Figure 7 shows the cumulative posterior probability for the radius and tidal deformability distribution of a $1.4M_{\odot}$ star similar to Fig. 5. The red and green colors indi-

cate results derived from the two sets of 10 events from our population. The solid lines indicate analyses derived using the same waveform model used to generate our synthetic signals (here, TEOBRESUMS). These two results are very similar, with modest differences in the posterior distribution due to the specific choice of ten events used in the analysis. Notably, the median of both distributions is nearly identical: for TEOBRESUMS, the median difference between the two realizations is only $\Delta R_{0.5} = 0.05\text{km}$. By contrast, the dashed lines show the population results derived if each event is analysed with a different waveform model family (here, IMRPHENOMD_NRTIDALV2). Though neither analysis exhibits as extreme systematic bias as the cherry-picked analysis described above, these two analyses do demonstrate that even a small-sample analysis generally incorporates a significant unmodeled systematic error. For example, the medians of the two dotted lines differ visibly and in a statistically significant way from one another and from the (common) median of the TEOBRESUMS analyses shown with solid lines. To be concrete, the median difference between the two IMRPHENOMD_NRTIDALV2 realizations is 0.5km – ten times larger than the difference for TEOBRESUMS – and are roughly ± 0.25 from the common median seen for TEOBRESUMS. Though smaller than the width of each posterior distribution, which accounts only for statistical uncertainty, this comparison demonstrates that waveform systematics introduce excess noise and that a few-event analysis can resolve its effect.

D. Discussion and ansatz

From the above analyses, we conclude that substantial waveform systematic uncertainties exist across the model space, exemplified by ubiquitous differences in marginal likelihoods and pertinent posteriors. Further, based on a census of our cross-waveform differences, we further anticipate that (as in prior work) these differences depend strongly on each specific event’s intrinsic (and potentially extrinsic) parameters. As a result, waveform systematics have two qualitatively different impacts on our inferences of the NS radius. First, they introduce a bias in our inferred radius, to the extent that each event on average contributes to a mean offset in $R_{1.4}$. By construction, this bias reflects the population average of the (unknown) systematic bias ΔR over the merging NS population. Second, because different events in the NS population produce different realizations of the systematic offset ΔR , for any specific set of events chosen, we will infer different answers for the radius. Asymptotically and assuming that second moments of ΔR exist, these realization-specific differences should converge to $\sigma_{\Delta R}/\sqrt{N}$, where σ_R is the population-averaged standard deviation of the bias ΔR .

Our numerical examples above are both consistent with this picture, and suggest that the population-averaged bias $\langle \Delta R \rangle$ is small, compared to the excess dis-

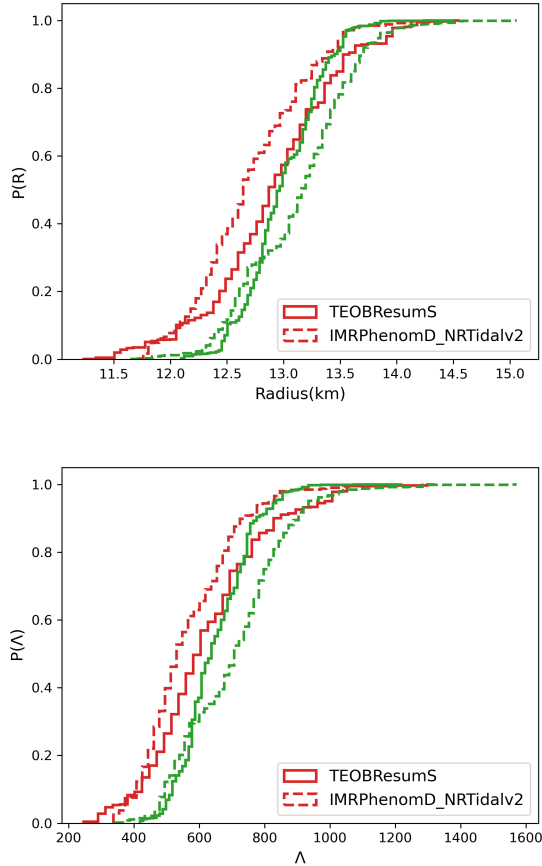


FIG. 7. *Top panel:* Histogram of the radius of a $1.4M_{\odot}$ neutron star for the equations-of-state realizations from the joint population and EoS inference. *Bottom panel:* Histogram of the dimensionless tidal deformability of a $1.4M_{\odot}$ neutron star for the equations-of-state realizations from the joint population and EoS inference. Legend indicates the waveform model used in the PE for the respective population analyses.

person from the standard deviation $\sigma_{\Delta R}$ of ΔR over our population. Our observation differs from multiple previous attempts to identify systematic biases from similar end-to-end population inference calculations. In brief and as discussed below, previous investigations usually examined a single sequence of BNS mergers, interpreting their $R(N)$ trajectory and particularly its endpoint as a measure of the average bias $\langle \Delta R \rangle$. By contrast, our calculations suggest that hundreds of BNS mergers should be analyzed self-consistently to resolve the systematic realization dependent error ($\sigma_{\Delta R}/\sqrt{N}$) from the expected population-averaged waveform bias $\langle \Delta R \rangle$, for the populations considered here.

Finally, the above ansatz suggests that the key parameters $\langle \Delta R \rangle$ and σ_R can be measured from the underlying parameter inference and propagated into population studies. As discussed earlier, in principle the pertinent differences which propagate into population-inferred

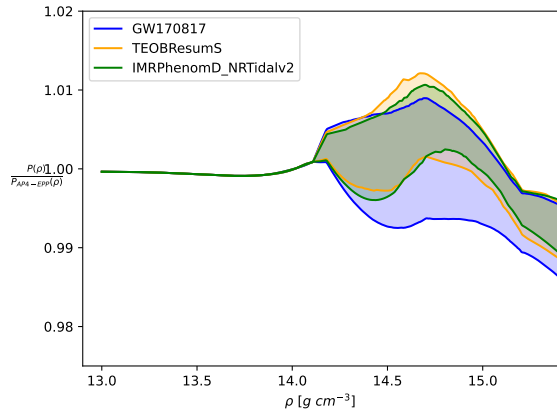


FIG. 8. Pressure-density plot comparing population analyses results from the different parameter estimation results performed for the same TEOBRESUMS-lmax4 injection, waveform model indicated in the legend. Specifically, it plots the ratio of pressure estimates from the recovered EoSs to that of pressure estimates from the injected equation-of-state, APR4. The shaded region indicates the 90% CI of the respective analyses.

EOS constraints arise in the underlying parameters inferences only from changes at small Λ . In practice and as a first approximation to characterize trends in systematics across the source binary parameter space, we will instead measure changes in the median value of Λ inferred for each event under the fiducial parameter inference prior. While this estimates for Λ are derived using an overly conservative and uninformative prior for the binary components masses and tides, we anticipate that it will nonetheless capture the dominant trend – rapid variation in ΔR across the binary parameter space, which over the population nearly averages to zero but with large variance.

E. Quantifying dispersion in $R_{1.4}$ and $\Lambda_{1.4}$

To understand the dispersion of the recovered $R_{1.4}$ and $\Lambda_{1.4}$ posterior distributions for different sub-sets of the injected population, we use a simple model of estimating the error of a quantity when multiple observations/data is stacked. For this, we choose to compute this quantity for the radius of a $1.4M_{\odot}$ neutron star from parameter estimation samples, using Eq.18 in Zhao & Lattimer [55], defined below:

$$R_{1.4} \simeq (11.5 \pm 0.3) \frac{\mathcal{M}}{M_{\odot}} \left(\frac{\tilde{\Lambda}}{800} \right)^{1/6} \quad (6)$$

Applying this expression to the median value of $\tilde{\Lambda}$ derived using the two different waveform models TEOBRESUMS and IMRPHENOMD_NRTIDALV2, we can furthermore for each event estimate a per-event estimate of difference

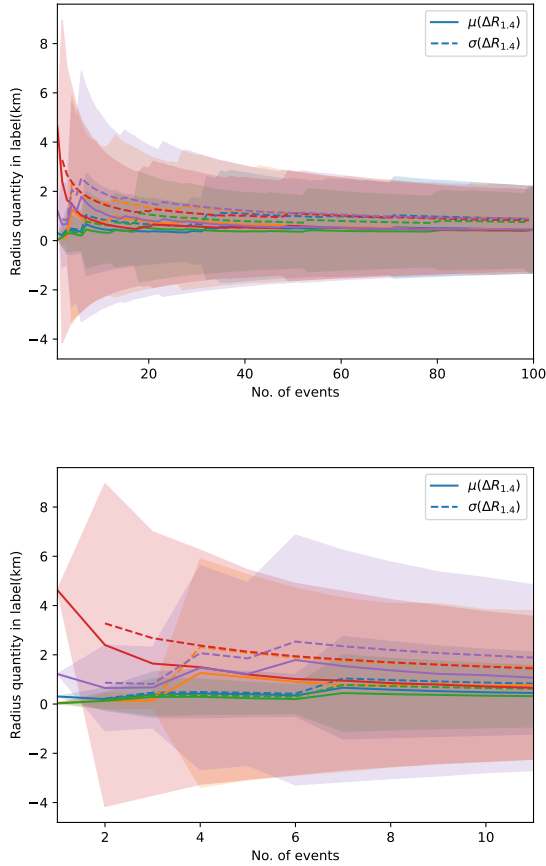


FIG. 9. *Top panel:* Plot showing how different stacking realizations of the 100-event simulated population converge to the same ΔR and its corresponding standard deviation after consideration of a certain high number of events. The shaded region shows the $\pm 2\sigma$ region of $\mu(\Delta R)$ for each realization. *Bottom panel:* Same plot as the top panel with the x-axis zoomed in to show the behavior for $N=10$ events.

in radius solely due to systematic waveform differences:

$$\Delta R_{1.4} = R_{1.4}^{\text{TEOBRESUMS}} - R_{1.4}^{\text{IMRPHENOMD_NRTIDALV2}} \quad (7)$$

The quantity $\Delta R_{1.4}$ varies substantially on a per-event basis, in part due to changes in systematic biases over the parameter space. For any subset of N events, we compute the sample mean $\bar{\Delta R} = \sum \Delta R_{1.4}/N$ and sample standard deviation $s_{\Delta R}$. For a sufficiently large sample, these two quantities should converge to the population-averaged mean $\mu_{\Delta R}$ and standard deviation $\sigma_{\Delta R}$ of ΔR .

Figure 9 shows the sample mean (solid curves) and sample standard deviation (dashed lines) of ΔR derived from different sample realizations, with the x axis indicating the number of samples used and the y axis measuring these two quantities (in km). Going from left to right, each solid-colored line calculates the sample mean using the first N events of a specific ordering of our 100 synthetic events. The different colors reflect five different choices of ordering.

At the right side of the graph, all estimates converge to an estimate of the true population-averaged mean $\mu_{\Delta R} \simeq 0.44\text{km}$ and true population-averaged standard deviation $\sigma_{\Delta R} \simeq 0.88\text{km}$. [In these estimates, we have not attempted any corrections to account for finite sample size.] Using these two parameters, we anticipate that for sufficiently large N , the sample mean $\bar{\Delta R}_{1.4}$ should have mean $\mu_{\Delta R}$ and standard deviation $\sigma_{\Delta R}/\sqrt{N}$. The shaded region shows the $\pm 2\sigma$ region of the sample mean, computed for each realization.

We emphasize that the differences characterized here with a random variable arise due to waveform systematics whose impact changes across the binary parameter space.

In terms of these empirical measurements characterizing systematic uncertainties, we anticipate that for an analysis comparable to Figure 5 – using $N = 10$ events – we would expect to see inferences derived using these two different waveform models to have medians that vary roughly according to a normal distribution with standard deviation comparable to $\sigma_{\Delta R_{1.4}}/\sqrt{N} \simeq 0.27\text{km}$ and systematic average error of order 0.4km . Notably, the difference in median is in good qualitative agreement with the features seen in Figure 5. Furthermore, for $N = 10$ events we find $\sigma_{\Delta R_{1.4}}/\sqrt{N}$ is comparable to $\mu_{\Delta R}$. As a result, we expect that with only tens of events, the posterior mean may very significantly solely due to the specific choice of 10 events selected, consistent with the findings shown in Figure 5. Only with a large sample size can we disentangle the relative contributions of mean and random systematic error.

IV. DISCUSSION

There have been multiple approaches to understanding the impact of GW modeling systematics on the inferred EoS derived from multiple GW observations. Kunert and collaborators [56] looked at the effect of waveform systematics on EoS inference when combining information from multiple detections for EoS inference from a discrete a priori grid, fixing a uniform NS population model. Their study used a fixed set of 38 synthetically-detected events, drawn from a uniformly distributed sample from their population model and volume, using an SNR threshold of 7. They performed population inference for the EOS, as characterized by $R_{1.4}$, for populations of 1 to 38 events, obtained by consecutively increasing their sample size by one. They repeated this approach 1000 different times, using different orderings of their 38 events (see, e.g., their Fig 2). As a result, for N sufficiently small compared to their total sample set, this study did use multiple randomly chosen synthetic universes from a larger sample [1]; however, their overall final results for systematic biases relies on a single set of 38 events. Like our work, they found that the result of their population inference depended on the choice of waveform model used to interpret the events, with shifts of up to 400m depending on the waveform used. They

demonstrated that a large sample size (here, their 38 events) was needed before these systematics were comparable to the posterior’s width. [The posterior incorporates only statistical uncertainty, not systematic uncertainty.] However, due to the limitations of a single data realization, unlike our work and some others [1] Kunert et al. does not characterize the increased dispersion that occurs due to waveform systematics, or discuss its impact on their final $N = 38$ fixed-sample-size analysis. Rather than producing a single unique bias, our study shows that (as should be expected) systematics also contributes to enhanced dispersion of the posterior, allowing for multiple realizations. In fact, the result of Kunert et al. for $N = 38$ is consistent with the same scale of random systematic dispersion suggested in our analysis. Their asymptotic result, which relies on a single realization, could reflect the true mean or instead dispersion.

Kunert and collaborators [56] also demonstrate that even though the net effects of waveform systematics for joint EoS inference are significant, on a per-event basis these systematic biases are relatively small compared to the per-event source parameter posterior. This conclusion has been corroborated by other studies like Gamba et al. [57], who argue that on a per-event basis systematic uncertainties will only be significant for sources with $\text{SNR} \geq 80$. In our investigation, however, the maximum SNR of an event is ~ 50 .

An article by Chatziioannou [58] uses physics-based analysis derived from the underlying gravitational wave phase to investigate different effects that could lead to uncertainties in the neutron star radius measurements. Her semianalytic analysis suggests that, with the current detectors and observations, the statistical uncertainties are a bigger factor than systematic uncertainties in determining the equation-of-state. These uncertainties start becoming comparable once a statistical error of 0.5-1 km is reached at the 90% credible level with A+ sensitivity. Pratten et al. [59] looks at the effect of exclusion of dynamical tides on the EoS reconstruction on a population of BNS, but one that is limited to lower-mass centered around $1.33M_{\odot}$. Although they see $\mathcal{O}(1 \text{ km})$ systematic differences in the recovered radius with `TaylorF2`, it is possible that using waveform models with higher-order models included could be responsible for better constraints and smaller error bars in our case.

Neither of the studies mentioned above performs a joint inference of the population properties of BNS sources along with the equation of state, which could bias the understanding of the inferred EoS, as demonstrated in [1, 33, 34]. Irrespective of that, there is a surprising consensus that the systematics are comparable to statistical effects in the order of 10 events, seen by us, Kunert et al. [56] and Chatziioannou [58].

V. CONCLUSIONS

In this paper, we investigated the impact of waveform systematics on a joint population and equation-of-state inference for a fiducial population of moderate-amplitude binary neutron star sources. Similar to [35], firstly, we use JS-divergences to quantify differences in the parameter estimation analysis, with a figure to illustrate a single extreme example from our large sample. Further, we use these posterior samples to perform multiple joint hierarchical inferences of the population and EoS properties of the fiducial systems by selecting different synthetic universes of ten of these events, following previous work [1]. We found that when the ten events are picked such that they have the worst JS divergence between the two waveform models, then the inferred EOS has a large systematic difference compared to the statistical error. We also performed a similar population analysis, choosing events at random and observing a more modest and random systematic difference between the inferred EOS. In other words, the systematically different events introduce downstream uncertainties into any calculations into which they are incorporated, increasing the systematic dispersion of EOS inferences.

To the best of our knowledge, this is one of the first works to propagate systematic error in end-to-end BNS EOS inference, accounting for multiple data realizations and using a sufficiently large sample, allowing us to probe better the long tail of rare but large differences between different waveform models in the NS parameter space. In the future, we plan to use this for future detections of BNS sources as well as make improvements in our current setup, such as combining information from neutron star-black hole (NSBH) sources.

ACKNOWLEDGMENTS

The authors would like to thank Anarya Ray for helpful comments. ROS gratefully acknowledges support from NSF awards NSF PHY-1912632, PHY-2012057, AST-1909534, and the Simons Foundation. AY acknowledges support from NSF PHY-2012057 grant. This material is based upon work supported by NSF’s LIGO Laboratory which is a major facility fully funded by the National Science Foundation. This research has made use of data, software and/or web tools obtained from the Gravitational Wave Open Science Center, a service of LIGO Laboratory, the LIGO Scientific Collaboration and the Virgo Collaboration. LIGO Laboratory and Advanced LIGO are funded by the United States National Science Foundation (NSF) as well as the Science and Technology Facilities Council (STFC) of the United Kingdom, the Max-Planck-Society (MPS), and the State of Niedersachsen/Germany for support of the construction of Advanced LIGO and construction and operation of the GEO600 detector. Additional support for Advanced LIGO was provided by the Australian Research

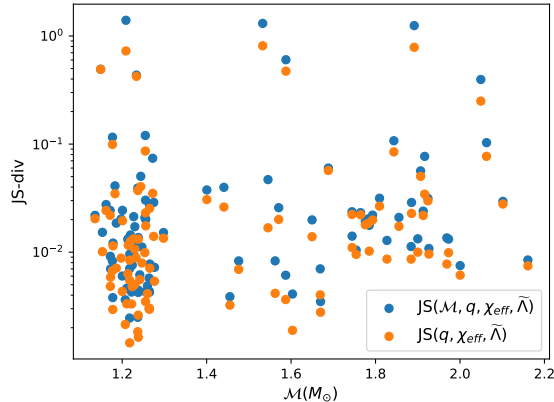


FIG. 10. Scatter plot showing how the chirp mass of the injections from the population relates to the JS divergence value between TEOBRESUMS and IMRPHENOMD_NRTIDALV2 samples for the parameters noted in the legend.

Council. Virgo is funded through the European Gravitational Observatory (EGO), by the French Centre National de Recherche Scientifique (CNRS), the Italian Istituto Nazionale di Fisica Nucleare (INFN), and the Dutch Nikhef, with contributions by institutions from Belgium, Germany, Greece, Hungary, Ireland, Japan, Monaco, Poland, Portugal, Spain. The authors are grateful for computational resources provided by the LIGO Laboratory and supported by National Science Foundation Grants PHY-0757058, PHY-0823459, PHY-1626190 and PHY-2110594. We acknowledge the use of IUCAA LDG cluster Sarathi for the computational/numerical work.

Appendix A: Chirp mass and JS divergence

Similar to Fig. 2 (bottom panel), we plotted the chirp-mass of the system against the JS divergence values of parameter inference samples of the two waveform models, and do not observe any correlation.

-
- [1] D. Wysocki, R. O’Shaughnessy, L. Wade, and J. Lange, Inferring the neutron star equation of state simultaneously with the population of merging neutron stars, (2020), arXiv:2001.01747 [gr-qc]
- [2] B. Abbott et al. (The LIGO Scientific Collaboration), Advanced LIGO, CQG **32**, 074001 (2015), arXiv:1411.4547 [gr-qc]
- [3] F. Acernese et al. (VIRGO), Advanced Virgo: a second-generation interferometric gravitational wave detector, Class. Quant. Grav. **32**, 024001 (2015), arXiv:1408.3978 [gr-qc]
- [4] T. Akutsu et al. (KAGRA), Overview of KAGRA: Detector design and construction history, PTEP **2021**, 05A101 (2021), arXiv:2005.05574 [physics.ins-det]
- [5] The LIGO Scientific Collaboration, The Virgo Collaboration, B. P. Abbott, R. Abbott, T. D. Abbott, F. Acernese, K. Ackley, C. Adams, T. Adams, P. Addesso, and et al., GWTC-1: A Gravitational-Wave Transient Catalog of Compact Binary Mergers Observed by LIGO and Virgo during the First and Second Observing Runs, PRX **9**, 031040 (2019)
- [6] The LIGO Scientific Collaboration, the Virgo Collaboration, R. Abbott, T. D. Abbott, S. Abraham, F. Acernese, K. Ackley, A. Adams, C. Adams, R. X. Adhikari, V. B. Adya, C. Affeldt, and et al., GWTC-2: Compact Binary Coalescences Observed by LIGO and Virgo during the First Half of the Third Observing Run, Physical Review X **11**, 021053 (2021), arXiv:2010.14527 [gr-qc]
- [7] R. Abbott, T. D. Abbott, F. Acernese, K. Ackley, C. Adams, N. Adhikari, R. X. Adhikari, V. B. Adya, C. Affeldt, D. Agarwal, and et al., GWTC-2.1: Deep extended catalog of compact binary coalescences observed by LIGO and Virgo during the first half of the third observing run, Phys. Rev. D **109**, 022001 (2024)
- [8] R. Abbott, T. D. Abbott, F. Acernese, K. Ackley, C. Adams, N. Adhikari, R. X. Adhikari, V. B. Adya, C. Affeldt, D. Agarwal, and et al., GWTC-3: Compact Binary Coalescences Observed by LIGO and Virgo during the Second Part of the Third Observing Run, Physical Review X **13**, 041039 (2023), arXiv:2111.03606 [gr-qc]
- [9] The LIGO Scientific Collaboration, The Virgo Collaboration, The KAGRA Scientific Collaboration, R. Abbott, T. D. Abbott, F. Acernese, K. Ackley, C. Adams, N. Adhikari, R. X. Adhikari, and et al., The population of merging compact binaries inferred using gravitational waves through GWTC-3, Available as arXiv:2111.03634, arXiv:2111.03634 (2021), arXiv:2111.03634 [astro-ph.HE]
- [10] The LIGO Scientific Collaboration, the Virgo Collaboration, B. P. Abbott, R. Abbott, T. D. Abbott, F. Acernese, K. Ackley, C. Adams, T. Adams, P. Addesso, and et al., GW170817: Observation of gravitational waves from a binary neutron star inspiral, Phys. Rev. Lett. **119**, 161101 (2017)
- [11] B. P. Abbott, R. Abbott, T. D. Abbott, et al., Gw190425: Observation of a compact binary coalescence with total mass $\sim 3.4 m_{\odot}$, ApJL **892**, L3 (2020)
- [12] B. P. Abbott et al. (LIGO Scientific, Virgo), Model comparison from LIGO–Virgo data on GW170817’s binary components and consequences for the merger remnant, Class. Quant. Grav. **37**, 045006 (2020), arXiv:1908.01012 [gr-qc]
- [13] B. P. Abbott et al. (LIGO Scientific, Virgo), GW170817: Measurements of neutron star radii and equation of state, Phys. Rev. Lett. **121**, 161101 (2018), arXiv:1805.11581 [gr-qc]
- [14] E. Annala, T. Gorda, A. Kurkela, and A. Vuorinen, Gravitational-wave constraints on the neutron-star-matter Equation of State, Phys. Rev. Lett. **120**, 172703 (2018), arXiv:1711.02644 [astro-ph.HE]
- [15] E. R. Most, L. R. Weih, L. Rezzolla, and J. Schaffner-Bielich, New constraints on radii and tidal deformabilities of neutron stars from GW170817, Phys. Rev. Lett. **120**, 261103 (2018), arXiv:1803.00549 [gr-qc]

- [16] M. Shibata, E. Zhou, K. Kiuchi, and S. Fujibayashi, Constraint on the maximum mass of neutron stars using GW170817 event, *Phys. Rev. D* **100**, 023015 (2019), arXiv:1905.03656 [astro-ph.HE]
- [17] C. Raithel, F. Özel, and D. Psaltis, Tidal deformability from GW170817 as a direct probe of the neutron star radius, *Astrophys. J. Lett.* **857**, L23 (2018), arXiv:1803.07687 [astro-ph.HE]
- [18] T. Dietrich, M. W. Coughlin, P. T. H. Pang, M. Bulla, J. Heinzl, L. Issa, I. Tews, and S. Antier, Multimessenger constraints on the neutron-star equation of state and the Hubble constant, *Science* **370**, 1450 (2020), arXiv:2002.11355 [astro-ph.HE]
- [19] M. W. Coughlin *et al.*, Constraints on the neutron star equation of state from AT2017gfo using radiative transfer simulations, *Mon. Not. Roy. Astron. Soc.* **480**, 3871 (2018), arXiv:1805.09371 [astro-ph.HE]
- [20] M. W. Coughlin, T. Dietrich, B. Margalit, and B. D. Metzger, Multimessenger Bayesian parameter inference of a binary neutron star merger, *Mon. Not. Roy. Astron. Soc.* **489**, L91 (2019), arXiv:1812.04803 [astro-ph.HE]
- [21] B. Margalit and B. D. Metzger, Constraining the Maximum Mass of Neutron Stars From Multi-Messenger Observations of GW170817, *Astrophys. J. Lett.* **850**, L19 (2017), arXiv:1710.05938 [astro-ph.HE]
- [22] G. Raaijmakers *et al.*, Constraining the dense matter equation of state with joint analysis of NICER and LIGO/Virgo measurements, *Astrophys. J. Lett.* **893**, L21 (2020), arXiv:1912.11031 [astro-ph.HE]
- [23] F. Özel, G. Baym, and T. Guver, Astrophysical Measurement of the Equation of State of Neutron Star Matter, *Phys. Rev. D* **82**, 101301 (2010), arXiv:1002.3153 [astro-ph.HE]
- [24] A. W. Steiner, J. M. Lattimer, and E. F. Brown, The Equation of State from Observed Masses and Radii of Neutron Stars, *Astrophys. J.* **722**, 33 (2010), arXiv:1005.0811 [astro-ph.HE]
- [25] J. M. Lattimer and A. W. Steiner, Neutron Star Masses and Radii from Quiescent Low-Mass X-ray Binaries, *Astrophys. J.* **784**, 123 (2014), arXiv:1305.3242 [astro-ph.HE]
- [26] A. L. Watts *et al.*, Colloquium : Measuring the neutron star equation of state using x-ray timing, *Rev. Mod. Phys.* **88**, 021001 (2016), arXiv:1602.01081 [astro-ph.HE]
- [27] M. C. Miller *et al.*, PSR J0030+0451 Mass and Radius from *NICER* Data and Implications for the Properties of Neutron Star Matter, *Astrophys. J. Lett.* **887**, L24 (2019), arXiv:1912.05705 [astro-ph.HE]
- [28] A. Kedia, R. O’Shaughnessy, L. Wade, and A. Yelikar, Exploring hidden priors when interpreting gravitational wave and electromagnetic probes of the nuclear equation of state, (2024), arXiv:2405.17326 [astro-ph.HE]
- [29] B. P. Abbott, R. Abbott, T. D. Abbott, S. Abraham, F. Acernese, K. Ackley, C. Adams, V. B. Adya, C. Affeldt, M. Agathos, and et al., Prospects for observing and localizing gravitational-wave transients with Advanced LIGO, Advanced Virgo and KAGRA, *Living Reviews in Relativity* **23**, 3 (2020)
- [30] The LIGO Scientific Collaboration, the Virgo Collaboration, B. P. Abbott, R. Abbott, T. D. Abbott, F. Acernese, K. Ackley, C. Adams, T. Adams, P. Addesso, and et al., GW170817: Measurements of neutron star radii and equation of state, *Phys. Rev. Lett.* **121**, 161101 (2018)
- [31] D. Wysocki and R. O’Shaughnessy, Bayesian parametric population models (2017–), [Online; accessed YYYY-MM-DD]
- [32] L. Lindblom, Spectral Representations of Neutron-Star Equations of State, *Phys. Rev. D* **82**, 103011 (2010), arXiv:1009.0738 [astro-ph.HE]
- [33] A. Ray, M. Camilo, J. Creighton, S. Ghosh, and S. Morisaki, Rapid hierarchical inference of neutron star equation of state from multiple gravitational wave observations of binary neutron star coalescences, *Phys. Rev. D* **107**, 043035 (2023), arXiv:2211.06435 [gr-qc]
- [34] J. Golomb and C. Talbot, Hierarchical Inference of Binary Neutron Star Mass Distribution and Equation of State with Gravitational Waves, *Astrophys. J.* **926**, 79 (2022), arXiv:2106.15745 [astro-ph.HE]
- [35] A. B. Yelikar, R. O. Shaughnessy, J. Lange, and A. Z. Jan, Waveform systematics in gravitational-wave inference of signals from binary neutron star merger models incorporating higher order modes information, (2024), arXiv:2404.16599 [gr-qc]
- [36] J. Lange, R. O’Shaughnessy, and M. Rizzo, Rapid and accurate parameter inference for coalescing, precessing compact binaries, Submitted to PRD; available at arxiv:1805.10457 (2018)
- [37] J. Wofford, A. B. Yelikar, H. Gallagher, E. Champion, D. Wysocki, V. Delfavero, J. Lange, C. Rose, V. Valsan, S. Morisaki, J. Read, C. Henshaw, and R. O’Shaughnessy, Improving performance for gravitational-wave parameter inference with an efficient and highly-parallelized algorithm, *Phys. Rev. D* **107**, 024040 (2023)
- [38] D. Wysocki, R. O’Shaughnessy, J. Lange, and Y.-L. L. Fang, Accelerating parameter inference with graphics processing units, *Phys. Rev. D* **99**, 084026 (2019), arXiv:1902.04934 [astro-ph.IM]
- [39] J. Lange, RIFT’ing the Wave: Developing and applying an algorithm to infer properties gravitational wave sources (2020)
- [40] T. Dietrich, A. Samajdar, S. Khan, N. K. Johnson-McDaniel, R. Dudi, and W. Tichy, Improving the NR-Tidal model for binary neutron star systems, *Phys. Rev. D* **100**, 044003 (2019), arXiv:1905.06011 [gr-qc]
- [41] T. Dietrich, S. Bernuzzi, and W. Tichy, Closed-form tidal approximants for binary neutron star gravitational waveforms constructed from high-resolution numerical relativity simulations, *Phys. Rev. D* **96**, 121501 (2017), arXiv:1706.02969 [gr-qc]
- [42] A. Nagar, S. Bernuzzi, W. Del Pozzo, G. Riemenschneider, S. Akcay, G. Carullo, P. Fleig, S. Babak, K. W. Tsang, M. Colleoni, F. Messina, G. Pratten, D. Radice, P. Rettengo, M. Agathos, E. Fauchon-Jones, M. Hannam, S. Husa, T. Dietrich, P. Cerdá-Duran, J. A. Font, F. Pannarale, P. Schmidt, and T. Damour, Time-domain effective-one-body gravitational waveforms for coalescing compact binaries with nonprecessing spins, tides, and self-spin effects, *Phys. Rev. D* **98**, 104052 (2018), arXiv:1806.01772 [gr-qc]
- [43] LIGO Scientific Collaboration, Advanced ligo anticipated sensitivity curves, (2018)
- [44] D. Wysocki, J. Lange, and R. O’Shaughnessy, Reconstructing phenomenological distributions of compact binaries via gravitational wave observations, *Phys. Rev. D* **100**, 043012 (2019)

- [45] F. Özel and P. Freire, Masses, Radii, and the Equation of State of Neutron Stars, *ARA&A* **54**, 401 (2016), arXiv:1603.02698 [astro-ph.HE]
- [46] J. Alsing, H. O. Silva, and E. Berti, Evidence for a maximum mass cut-off in the neutron star mass distribution and constraints on the equation of state, *MNRAS* **478**, 1377 (2018), arXiv:1709.07889 [astro-ph.HE]
- [47] L. Lindblom, Spectral representations of neutron-star equations of state, *Phys. Rev. D* **82**, 103011 (2010), arXiv:1009.0738 [astro-ph.HE]
- [48] M. F. Carney, L. E. Wade, and B. S. Irwin, Comparing two models for measuring the neutron star equation of state from gravitational-wave signals, *Phys. Rev. D* **98**, 063004 (2018), arXiv:1805.11217 [gr-qc]
- [49] LIGO Scientific Collaboration, LIGO Algorithm Library - LALSuite, free software (GPL) (2018)
- [50] D. R. Lorimer, Binary and Millisecond Pulsars, *Living Reviews in Relativity* **11**, 8 (2008), arXiv:0811.0762 [astro-ph]
- [51] J. Antoniadis, P. C. C. Freire, N. Wex, T. M. Tauris, R. S. Lynch, M. H. van Kerkwijk, M. Kramer, C. Bassa, V. S. Dhillon, T. Driebe, J. W. T. Hessels, V. M. Kaspi, V. I. Kondratiev, N. Langer, T. R. Marsh, M. A. McLaughlin, T. T. Pennucci, S. M. Ransom, I. H. Stairs, J. van Leeuwen, J. P. W. Verbiest, and D. G. Whelan, A Massive Pulsar in a Compact Relativistic Binary, *Science* **340**, 448 (2013), arXiv:1304.6875 [astro-ph.HE]
- [52] J. Antoniadis, T. M. Tauris, F. Özel, E. Barr, D. J. Champion, and P. C. C. Freire, The millisecond pulsar mass distribution: Evidence for bimodality and constraints on the maximum neutron star mass, arXiv e-prints (2016), arXiv:1605.01665 [astro-ph.HE]
- [53] H. T. Cromartie, E. Fonseca, S. M. Ransom, P. B. Demorest, Z. Arzoumanian, H. Blumer, P. R. Brook, M. E. DeCesar, T. Dolch, J. A. Ellis, R. D. Ferdman, E. C. Ferrara, N. Garver-Daniels, P. A. Gentile, M. L. Jones, M. T. Lam, D. R. Lorimer, R. S. Lynch, M. A. McLaughlin, C. Ng, D. J. Nice, T. T. Pennucci, R. Spiewak, I. H. Stairs, K. Stovall, J. K. Swiggum, and W. Zhu, Relativistic Shapiro delay measurements of an extremely massive millisecond pulsar, arXiv e-prints (2019), arXiv:1904.06759 [astro-ph.HE]
- [54] LIGO Scientific Collaboration, Virgo Collaboration and KAGRA Collaboration, *GW170817: Measurements of Neutron Star Radii and Equation of State*, Tech. Rep. DCC-P1800115 (2018)
- [55] T. Zhao and J. M. Lattimer, Tidal Deformabilities and Neutron Star Mergers, *Phys. Rev. D* **98**, 063020 (2018), arXiv:1808.02858 [astro-ph.HE]
- [56] N. Kunert, P. T. H. Pang, I. Tews, M. W. Coughlin, and T. Dietrich, Quantifying modeling uncertainties when combining multiple gravitational-wave detections from binary neutron star sources, *Phys. Rev. D* **105**, L061301 (2022), arXiv:2110.11835 [astro-ph.HE]
- [57] R. Gamba, M. Breschi, S. Bernuzzi, M. Agathos, and A. Nagar, Waveform systematics in the gravitational-wave inference of tidal parameters and equation of state from binary neutron star signals, *Phys. Rev. D* **103**, 124015 (2021), arXiv:2009.08467 [gr-qc]
- [58] K. Chatziioannou, Uncertainty limits on neutron star radius measurements with gravitational waves, *Phys. Rev. D* **105**, 084021 (2022), arXiv:2108.12368 [gr-qc]
- [59] G. Pratten, P. Schmidt, and N. Williams, Impact of Dynamical Tides on the Reconstruction of the Neutron Star Equation of State, *Phys. Rev. Lett.* **129**, 081102 (2022), arXiv:2109.07566 [astro-ph.HE]